Journal of Solid State Chemistry 273 (2019) 175–185

Contents lists available at ScienceDirect

Journal of Solid State Chemistry

journal homepage: www.elsevier.com/locate/jssc

Magnetic properties of $La_3Ni_2Sb_xTa_yNb_{1-x-y}O_9$; from relaxor to spin glass

Chun–Mann Chin [a], Peter D. Battle [a,*], Emily C. Hunter [a], Maxim Avdeev [b,c], Mylène Hendrickx [d], Joke Hadermann [d]

[a] Inorganic Chemistry Laboratory, Oxford University, South Parks Road, Oxford, OX1 3QR, UK
[b] Australian Nuclear Science and Technology Organisation, Lucas Heights, NSW2234, Australia
[c] School of Chemistry, The University of Sydney, NSW, 2006, Australia
[d] EMAT, University of Antwerp, Groenenborgerlaan 171, 2020, Antwerp, Belgium

ARTICLE INFO

Keywords:
Relaxor ferromagnet
Spin glass
Perovskite oxide

ABSTRACT

Neutron diffraction experiments conducted at 5 K in a magnetic field $0 \leq H/\text{kOe} \leq 50$ have shown that the monoclinic perovskite $La_3Ni_2TaO_9$ behaves as a relaxor ferromagnet. Compositions in the series $La_3Ni_2Sb_xTa_yNb_{1-x-y}O_9$ have been synthesized in polycrystalline form. Electron microscopy, X–ray diffraction and neutron diffraction have shown that the solid solutions are largely homogeneous and monophasic. Magnetometry and neutron diffraction have shown that the relaxor magnetisation persists in low fields when $x + y = 1$ but is rapidly diminished by the introduction of niobium. This change in magnetic behaviour is ascribed to the differences in the *d*–orbital energies of Sb^{5+}, Nb^{5+} and Ta^{5+}.

1. Introduction

Pseudo–cubic triple perovskites having the general formula $A_3B_2B'O_9$, where B is a paramagnetic cation and B' is a diamagnetic cation, show a wide range of magnetic properties. The available experimental evidence suggests that their behaviour depends not only on chemical factors, for example the composition, the electronic configurations of B and B' and the extent to which B and B' order over distinct crystallographic sites, but also on the microstructure, for example the concentration of twin planes. This can be illustrated by comparing the behaviour of $SrLa_2Ni_2TeO_9$, which has a partially–ordered distribution of d^8:Ni^{2+} and d^{10}:Te^{6+} cations and a complex microstructure [1], with that of $LaSr_2Cr_2SbO_9$, which has a partially–ordered distribution of d^3:Cr^{3+} and d^{10}:Sb^{5+} cations and a relatively simple microstructure [2]; the former shows many of the characteristics of a spin glass below 35 K whereas the latter is ferrimagnetic below ~150 K.

The behaviour of $La_3Ni_2SbO_9$ has been found to be particularly interesting. This compound adopts the monoclinic space group $P2_1/n$ and the ~5.5 × ~5.6 × ~7.8 Å unit cell contains two distinct six–coordinate sites. One is occupied entirely by Ni^{2+} and the other by the remaining Ni^{2+} (33%) and all the Sb^{5+} (66%). This is essentially the same ordering pattern as is found in $LaSr_2Cr_2SbO_9$, but in the case of $La_3Ni_2SbO_9$ the ordering, as judged by neutron diffraction, is complete rather than partial, *i.e.* Sb^{5+} cations are absent, within statistical error, from one of the two sites in the latter compound but not in the former [3]. The dominant superexchange interaction between nearest–neighbour Ni^{2+} cations along a nearly–linear superexchange pathway connecting the two sites is expected to be antiferromagnetic. It is therefore reasonable to expect the imbalance in the number of magnetic cations on the two sites to lead to ferrimagnetism, as it does in $LaSr_2Cr_2SbO_9$. Indeed, the magnetisation of $La_3Ni_2SbO_9$ increases markedly on cooling below 105 K and the ac susceptibility concomitantly becomes complex and frequency–dependent, as would be expected for a ferrimagnet. However, in contrast to $LaSr_2Cr_2SbO_9$, no magnetic Bragg scattering was detected in a neutron diffraction pattern collected at 5 K. In order to provide a self–consistent explanation of these observations it was postulated, by analogy with the relaxor ferroelectric $Pb_3MgNb_2O_9$ [4], that $La_3Ni_2SbO_9$ is a relaxor ferromagnet, i.e. within each crystallite, ferrimagnetic ordering occurs in multiple small domains but the magnetisation vectors within the different domains do not lie parallel to each other. The ordering is therefore not maintained over the distances sampled in a neutron diffraction experiment but the magnetisation of the sample increases sharply when the magnetisation vectors are aligned by an external magnetic field. It was subsequently shown [5] that magnetic Bragg scattering is observed when neutron diffraction data are collected in an applied field, i.e. when all the magnetisation vectors are aligned parallel throughout each crystallite. This second study recognised that weak magnetic Bragg scattering was in fact present in zero field, albeit much

* Corresponding author.
E-mail address: peter.battle@chem.ox.ac.uk (P.D. Battle).

https://doi.org/10.1016/j.jssc.2019.02.044
Received 23 January 2019; Received in revised form 27 February 2019; Accepted 27 February 2019
Available online 2 March 2019

less than would be expected from a fully–ordered material. It was attributed to the presence of a small number of relatively–large domains.

Although many $A_3B_2B'O_9$ compounds have been studied recently, $La_3Ni_2TaO_9$ [6] is the only one for which the magnetometry and out–of–field neutron diffraction data mimic those collected from $La_3Ni_2SbO_9$. Indeed, on careful inspection of the data, no magnetic scattering could be detected at low temperatures, suggesting that $La_3Ni_2TaO_9$ may be a better example of a relaxor ferromagnet than the Sb–containing composition. In view of this it is surprising that $La_3Ni_2NbO_9$ behaves as a spin glass [7], with no indication of either long–range magnetic order or relaxor properties, particularly since a study using transmission electron microscopy [6] (TEM) failed to identify any difference in the microstructures of the two compositions and showed that, in the case of our two samples, $La_3Ni_2NbO_9$ had the larger particle size. We describe below an in–field neutron diffraction experiment undertaken to confirm the relaxor character of $La_3Ni_2TaO_9$ and a study of the systems $La_3Ni_2Ta_yNb_{1-y}O_9$, $La_3Ni_2Sb_xTa_yO_9$ and $La_3Ni_2Sb_xNb_{1-x}O_9$ which was undertaken in an attempt to understand the factors that determine when relaxor behaviour will occur.

2. Experimental

2.1. $La_3Ni_2TaO_9$

Neutron powder diffraction (NPD) data were collected from $La_3Ni_2TaO_9$ in an applied magnetic field using the diffractometer Echidna [8] at ANSTO, Australia. The same sample that was used in our earlier, zero–field study [6] was made into a pellet which was then broken into fragments, each just small enough to be loaded into a standard vanadium container. This was done to prevent movement of the sample in the magnetic field. The vanadium container was then mounted in a vertical–field cryomagnet. Data were collected over the angular range $10 \leq 2\theta/^\circ \leq 158$ at 5 K in fields of 0, 4, 20 and 50 kOe using a neutron wavelength of 2.4395 Å. In order to study the reversibility of any change in the magnetic scattering a final pattern was recorded in 0 kOe after the magnet had been switched off. The NPD patterns were analysed using the Rietveld method [9] as implemented in the GSAS program suite [10]. The peak shape was modelled using a pseudo–Voigt function and the background was fitted with a 15–term shifted Chebyshev function. Regions where the patterns were contaminated by the aluminium in the cryomagnet were excluded from the refinements.

2.2. $La_3Ni_2Sb_xTa_yNb_{1-x-y}O_9$

Polycrystalline samples of compositions containing two pentavalent cations were prepared using the traditional ceramic method. Stoichiometric amounts of NiO, B'_2O_5 (B' = Sb, Nb or Ta) and pre–dried La_2O_3 were thoroughly mixed and ground in an agate mortar and pestle. Each mixture was pelletised and heated in air at 1200–1250 °C for up to 16 days. The pellet was ground and reformed every 2–4 days. In all, three new compositions in each of the three series Sb/Nb, Sb/Ta and Ta/Nb were prepared. X–ray powder diffraction (XRPD) was used to monitor the progress of the reactions and to characterise the final products. Data were collected at room temperature (RT) using a PANalytical Empyrean diffractometer with Cu $K_{\alpha 1}$ radiation ($\lambda = 1.54051$ Å). Powders were sprinkled onto a silicon wafer which was then mounted on a spinning sample holder. The sample was spun at a rate of one rotation per second during each data collection. Data were collected over an angular range of $15 \leq 2\theta/^\circ \leq 125$ with a step–size, $\Delta 2\theta$, of 0.0066°. The XRPD patterns were analysed using the Rietveld method, as implemented in the GSAS program suite. The background level of each pattern was modelled by a shifted Chebyshev function and the peak shapes were fitted with a pseudo–Voigt function.

A SQUID magnetometer was employed to study the magnetic properties of the $La_3Ni_2Sb_xTa_yNb_{1-x-y}O_9$ series. 30–50 mg of the sample was first cooled to 5 K in the absence of a magnetic field (Zero–Field Cooling, ZFC) and then the dc susceptibility was measured in a field of 100 Oe as the sample was warmed to 300 K. This was repeated after the sample had been cooled to 5 K in a field of 100 Oe (Field Cooling, FC). The field dependence of the magnetisation per formula unit (f.u.) was measured over the range $-50 \leq H/\text{kOe} \leq 50$ at 5, 150 and 220 K.

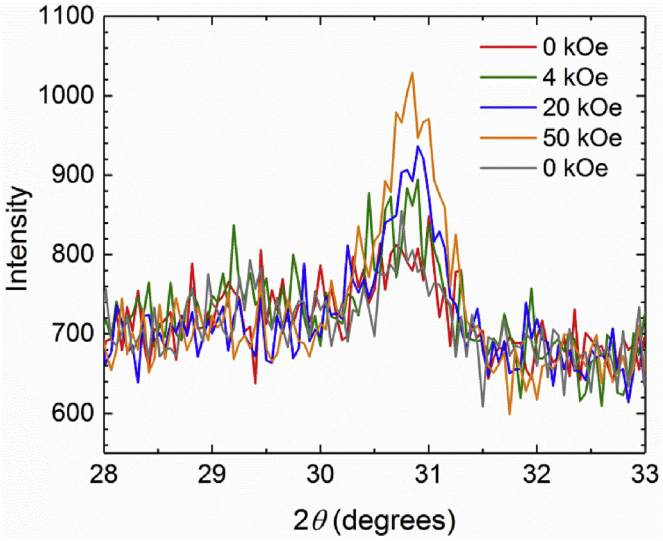

Fig. 1. Intensity of 011 reflection of $La_3Ni_2TaO_9$ at 5 K in applied magnetic fields of 0 (red), 4 (olive), 20 (blue), 50 (orange) and back to 0 (grey) kOe. (For interpretation of the references to colour in this figure legend, the reader is referred to the Web version of this article.)

All of the compositions containing two pentavalent cations were characterised by X–ray diffraction and dc magnetometry as described above. However, three of them (i.e. $La_3Ni_2Ta_{0.75}Nb_{0.25}O_9$, $La_3Ni_2Sb_{0.75}Ta_{0.25}O_9$ and $La_3Ni_2Sb_{0.75}Nb_{0.25}O_9$) were studied in greater detail using ac magnetometry, electron microscopy and neutron diffraction. Their ac susceptibilities were measured over the temperature range $2 \leq T/\text{K} \leq 150$ in a magnetic field of amplitude 3.5 Oe oscillating at frequencies of 1, 10, 100 and 1000 Hz.

The homogeneity of these selected reaction products was studied by performing low–magnification energy–dispersive X–ray (EDX) measurements on a 200 kV FEI Osiris microscope equipped with a Super–X detector. Specimens were prepared by dispersing a crushed polycrystalline sample in ethanol and depositing a few drops of this suspension on a copper grid covered with a holey carbon film. The L–lines were used for the quantification of La (~4.6 keV), Sb (~3.6 keV) and Nb (~2.2 keV) and the K–lines for the quantification of Ni (~1.7 keV). In the case of Ta there was a choice of two line series, the M–lines (~1.7 keV) and the L–lines (~8.1 keV), which overlap with Si peaks arising from the sample preparation or Cu peaks arising from the support, respectively. We chose to use the L–line for all measurements as there was less peak overlap compared to the M–line and it produced results closer to the expected stoichiometry. The oxygen content, which cannot be accurately quantified by EDX, was excluded from the analysis. The compositions of between 36 and 53 regions were measured across multiple grains of each sample in order to determine the average stoichiometry. In the light of the results of these experiments $La_3Ni_2Sb_{0.75}Ta_{0.25}O_9$ and $La_3Ni_2Sb_{0.75}Nb_{0.25}O_9$ were studied further. Selected area electron diffraction (SAED) patterns were taken with an FEI Tecnai G2 microscope and further HAADF–STEM images, along with high–resolution EDX (HR–EDX) maps were acquired with an FEI Titan 80–300 "cubed" microscope equipped with a Super–X detector and operated at 300 kV.

Neutron powder diffraction (NPD) patterns of $La_3Ni_2Ta_{0.75}Nb_{0.25}O_9$, $La_3Ni_2Sb_{0.75}Ta_{0.25}O_9$ and $La_3Ni_2Sb_{0.75}Nb_{0.25}O_9$ were recorded using the diffractometer Echidna. Data were collected at RT and 3.5 K (3 K in the case of $La_3Ni_2Sb_{0.75}Nb_{0.25}O_9$). The measurements covered an angular range of $10 \leq 2\theta/^\circ \leq 158$ with $\Delta 2\theta = 0.05^\circ$ and used a wavelength of

Table 1
Magnetic parameters of $La_3Ni_2Sb_xNb_{1-x}O_9$.

x	μ_{eff}/μ_B	θ_W/K	M_R/μ_B	H_C/kOe	T_C/K	T_{MAX}/K
1	2.08(1)	+164(2)	0.5	0.46	100	45
0.75	2.07(1)	+166(2)	0.51	0.38	100	45
0.5	2.09(1)	+156(3)	0.36	0.46	95	40
0.25	2.10(1)	+149(2)	0.22	0.76	80	35
0	2.10(1)	+140(1)	0.1	1.3	29	29

Table 2
Magnetic parameters of $La_3Ni_2Sb_xTa_yO_9$.

x:y	μ_{eff}/μ_B	θ_W/K	M_R/μ_B	H_C/kOe	T_C/K	T_{MAX}/K
1:0	2.08(1)	+164(2)	0.5	0.46	100	45
0.75:0.25	2.11(1)	+163(3)	0.51	0.4	105	50
0.5:0.5	2.08(1)	+159(2)	0.42	0.4	100	45
0.25:0.75	2.07(1)	+155(2)	0.4	0.4	95	45
0:1	2.13(1)	+146(1)	0.2	0.6	85	35

Table 3
Magnetic parameters of $La_3Ni_2Ta_yNb_{1-y}O_9$.

y	μ_{eff}/μ_B	θ_W/K	M_R/μ_B	H_C/kOe	T_C/K	T_{MAX}/K
1	2.13(1)	+146(2)	0.2	0.6	85	35
0.75	2.07(1)	+147(2)	0.2	0.66	70	35
0.5	2.11(1)	+144(2)	0.16	0.83	33	33
0.25	2.10(1)	+139(1)	0.12	1.1	32	32
0	2.10(1)	+140(1)	0.1	1.3	29	29

either 1.622 or 2.4395 Å. The data collected using the shorter and longer wavelengths were primarily for use in the analysis of the nuclear and magnetic Bragg scattering, respectively. The NPD patterns were analysed by the Rietveld method as implemented in GSAS.

3. Results

3.1. $La_3Ni_2TaO_9$

The structural model derived in our earlier study [6] was employed in the analysis of the NPD data collected at ANSTO. When a magnetic field was applied, the intensity of the 011 Bragg reflection at $2\theta \sim 31^\circ$ increased with increasing field strength, see Fig. 1. The additional intensity could be accounted for by assuming that the field causes the Ni^{2+} cations on the 2*c* and 2*d* sites to order in a G–type magnetic structure that is with nearest–neighbour cations having antiparallel moments. With the magnetic sublattice being pseudo–cubic, the magnetic moment of the Ni^{2+} cation was arbitrarily assigned to be along the *c* axis. The magnitude of the magnetic moment of Ni^{2+} was refined by Rietveld analysis of the in–field diffraction patterns. The moment was found to be 0.79(9), 1.07(7) and 1.34(6) μ_B per Ni^{2+} cation in fields of 4, 20 and 50 kOe, respectively. The diffraction pattern collected after the magnetic field had been switched off could be superimposed on the initial, zero–field pattern, showing that the magnetic field had not caused re–orientation of the grains of powder.

3.2. $La_3Ni_2Sb_xTa_yNb_{1-x-y}O_9$

3.2.1. X–ray diffraction

The XRPD patterns collected from the reaction products containing two pentavalent cations were dominated by a monoclinic, perovskite–like phase which adopts the space group $P2_1/n$ with $a \sim b \sim \sqrt{2}a_p$, $c \sim 2a_p$, $\beta \sim 90^\circ$ where a_p is the unit cell parameter of a primitive cubic perovskite. Some compositions were contaminated by a small trace of $LaTa_pNb_{1-p}O_4$ (<1 wt %). The crystal structure of the perovskites thus contains two crystallographically distinct octahedral sites, 2*c* and 2*d*. In our initial analysis of the cation distribution over the two six–coordinate sites the coordinates of the weakly–scattering oxide ions were not refined and it was assumed there was no site ordering between the different pentavalent cations. These Rietveld refinements showed that the 2*c* site of all the compositions is mainly occupied by the larger Ni^{2+} cation (≥95%) while the remaining Ni^{2+} cations share the 2*d* site with the pentavalent cations that are present. The distribution of the *B*′ cations was then allowed to vary whilst the occupancy of Ni^{2+} over the two sites was held constant in order to establish whether there was any ordering among the pentavalent cations. These refinements did not yield any significant improvement in the fits and our XRPD data thus provide no evidence for long–range site ordering among the different species of pentavalent *B*′ cations (Nb/Ta, Sb/Ta or Sb/Nb). Fitted XRPD patterns of selected compositions are shown in Fig. S1; the unit cell parameters of those not discussed in more detail below are listed in Table S1.

3.2.2. Magnetometry

The temperature dependence of the dc molar susceptibility and the inverse susceptibility of each composition studied is shown in Figs. S2 – S4. In every case $\chi(T)$ reaches a maximum value at a temperature $T_{max} < 60$ K, see Tables 1–3, and the ZFC and FC susceptibilities differ below this temperature; in some cases a difference is also apparent at temperatures between T_{max} and 100 K. $\chi^{-1}(T)$ of all the compositions except $La_3Ni_2Sb_{0.75}Nb_{0.25}O_9$ is linear above 220 K (240 K in the case of $La_3Ni_2Sb_{0.75}Nb_{0.25}O_9$), indicating that they become paramagnetic on warming. The data collected in the linear region of $\chi^{-1}(T)$ were fitted to the Curie–Weiss Law in order to derive the effective magnetic moment of each Ni^{2+} cation, μ_{eff}, and the Weiss temperature, θ_W, which are listed in Tables 1–3. The field dependence of the magnetisation per formula unit (f.u.), $M(H)$, at selected temperatures is also shown in Figs. S2 – S4. At 5 K, hysteresis is apparent in every compound. The values of the coercive field (H_C) and remanent magnetisation (M_R) observed at this temperature are included in Tables 1–3. Hysteresis is not apparent in $M(H)$ at 150 or 220 K although the function is nonlinear at the lower of these temperatures. The composition dependence of the FC susceptibility and $M(H)$ at 5 K within each solid solution can be seen in Figs. 2 and 3.

The temperature and frequency dependence of the ac molar susceptibility of $La_3Ni_2Ta_{0.75}Nb_{0.25}O_9$, $La_3Ni_2Sb_{0.75}Ta_{0.25}O_9$ and $La_3Ni_2Sb_{0.75}Nb_{0.25}O_9$ are illustrated in Fig. 4. The data from the latter two compositions show the same general features. The real component, χ', increases relatively smoothly with temperature between 2 K and ~90 K and is frequency–dependent above 30 K. The positive slope of $\chi'(T)$ becomes steeper above ~90 K and the function reaches a well–defined maximum at a frequency–independent temperature of 95 K before falling sharply as the temperature increases to ~100 K. The imaginary component χ'' is an order of magnitude weaker but shows the same general features as χ'. However, a change in gradient can be observed in the former at approximately 50 K, indicating the possibility of a second magnetic transition. The behaviour of $La_3Ni_2Ta_{0.75}Nb_{0.25}O_9$ is very different to that of the two Sb–containing compositions. $\chi'(T)$ and $\chi''(T)$ are frequency–dependent over the temperature range $20 < T/K < 75$ and both show a broad maximum at a frequency–independent temperature of ~50 K.

3.2.3. Electron microscopy

The cation compositions derived from low–magnification EDX maps collected from the three samples chosen for more detailed study were $La_{0.52(1)}Ni_{0.31(1)}Ta_{0.13(2)}Nb_{0.04(2)}$ (*38*), $La_{0.51(1)}Ni_{0.30(1)}Sb_{0.12(2)}Ta_{0.06(2)}$ (*36*) and $La_{0.52(1)}Ni_{0.30(1)}Sb_{0.14(2)}Nb_{0.04(2)}$ (*53*); the italicized figure in brackets is the number of regions analysed in each case. These formulations are in reasonable agreement with the targeted compositions, although the La and Ni contents are systematically high and low, respectively. The standard deviations indicate that while there is little variation in the atomic percentage of La and Ni in the different grains there is a greater deviation in the proportion of each of the two B′ cations present. Fig. 5, Figs. S5 and S6 show a representative EDX map of a grain

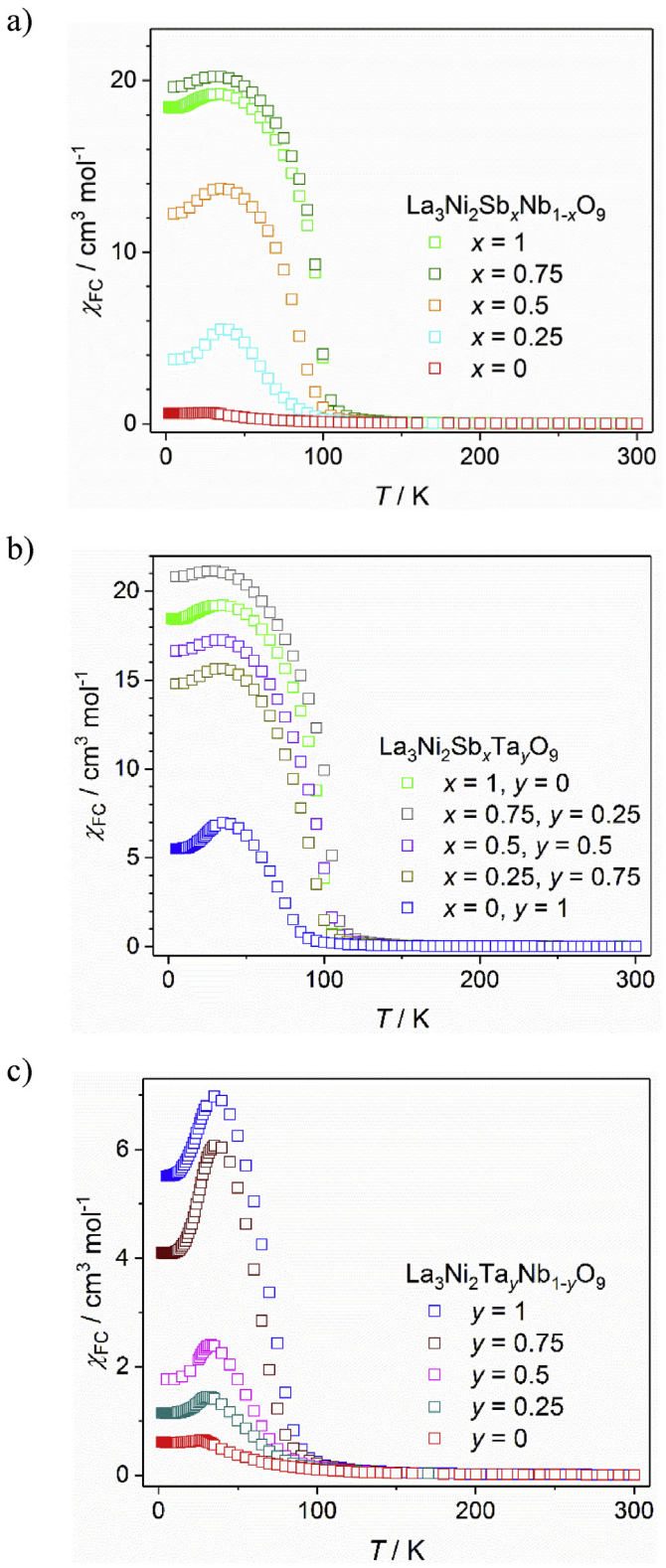

Fig. 2. Temperature dependence of the FC molar susceptibility of (a) $La_3Ni_2Sb_xNb_{1-x}O_9$, (b) $La_3Ni_2Sb_xTa_yO_9$ and (c) $La_3Ni_2Ta_yNb_{1-y}O_9$.

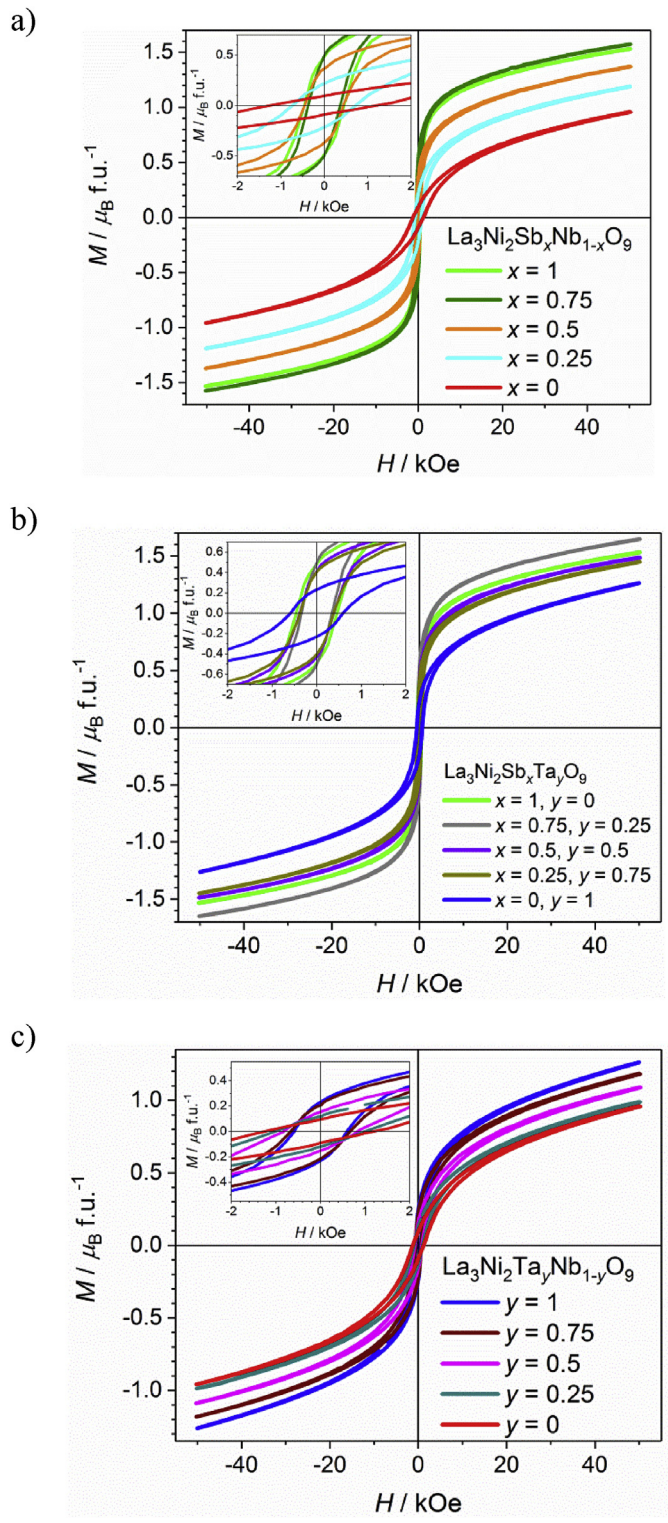

Fig. 3. Field dependence of the magnetisation per formula unit of (a) $La_3Ni_2Sb_xNb_{1-x}O_9$, (b) $La_3Ni_2Sb_xTa_yO_9$ and (c) $La_3Ni_2Ta_yNb_{1-y}O_9$ at 5 K. The insets show the same function for $-2 < H/\text{kOe} < 2$.

from each sample. In the two Sb–containing samples there were a few grains, exemplified by the arrowed regions in Fig. 5, where the ratio of the B′–site cations is inverted; no such extreme variations were seen in the Nb/Ta sample. Despite the compositional fluctuations, the overall ratio of the Ni to the B′ cations remains 2:1 within error. Following the observation of regions in which the concentration of pentavalent cations was inverted, SAED patterns were collected from the two Sb–containing compositions along the zone axes [100], [010], [001], [110] and [201], see Fig. 6, and Fig. S7. All the SAED patterns could be indexed using the cell parameters: $a \approx b \approx \sqrt{2}a_p$, $c \approx 2a_p$ and $\beta \approx 90°$, and showed the following reflection conditions: *hkl, 0kl, hk0: no conditions; h0l, h00, 00l:*

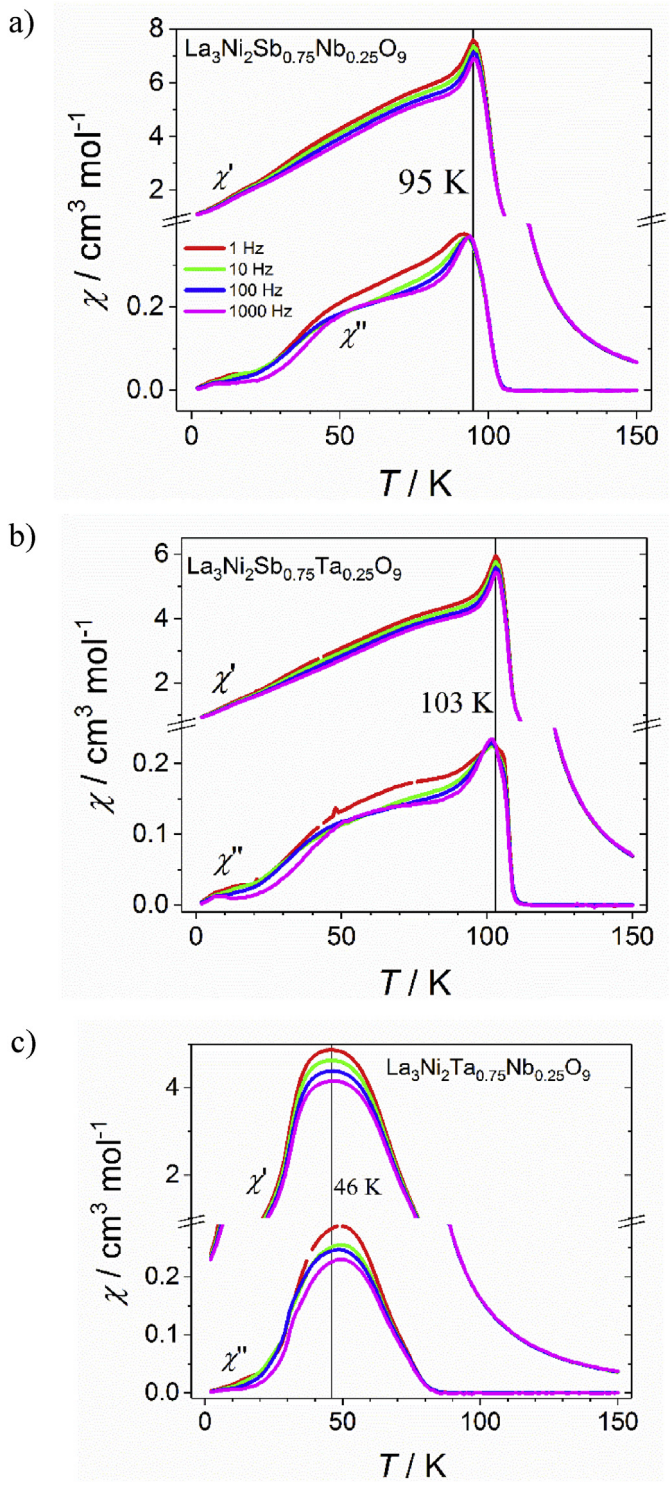

Fig. 4. The temperature and frequency dependence of the real and imaginary components of the ac molar susceptibility of (a) $La_3Ni_2Sb_{0.75}Nb_{0.25}O_9$, (b) $La_3Ni_2Sb_{0.75}Ta_{0.25}O_9$ and (c) $La_3Ni_2Ta_{0.75}Nb_{0.25}O_9$ collected at 1 (red), 10 (green), 100 (blue) and 1000 (magenta) Hz. (For interpretation of the references to colour in this figure legend, the reader is referred to the Web version of this article.)

$h + l = 2n$; *0k0:* $k = 2n$. Reflections in conflict with the reflection conditions: *h00, 0k0, 00l: h, k,* $l = 2n$ *and h0l:* $h + l = 2n$, are present in the [100], [001], [110] and [201] SAED patterns but are due to double diffraction; this was verified by tilting the crystal out of zone around the relevant axes. These reflection conditions and cell parameters show that $La_3Ni_2Sb_{0.75}Nb_{0.25}O_9$ and $La_3Ni_2Sb_{0.75}Ta_{0.25}O_9$ adopt the monoclinic space group $P2_1/n$, in agreement with the X–ray data described above. The HR–EDX maps collected from areas of $La_3Ni_2Sb_{0.75}Nb_{0.25}O_9$ and $La_3Ni_2Sb_{0.75}Ta_{0.25}O_9$ with the expected composition show a clear 1:1 order between Ni and B' in that Ni fully occupies one B site and the other is occupied by the remaining Ni and the two B' cations, see Fig. 7, and Fig. S8. An atomic resolution EDX map from a region of inverted B' composition in $La_3Ni_2Sb_{0.75}Ta_{0.25}O_9$, see Fig. 8, shows that the same 1:1 ordering occurs in the inverted composition with one B site being fully occupied by Ni and the other by Ni, Sb and Ta. The 1:1 ordering of the B–site cations can also be clearly observed in the HAADF–STEM images of both compounds taken along the [010] orientation, as shown in Fig. 9 and Fig. S9. The brightness of the dots in the HAADF–STEM images increases with the increasing total atomic number, Z, of the column. The continuous rows of dots along the a–axis correspond to the A sites occupied by La. The rows with alternation of darker and brighter dots along the x–axis correspond to the alternating Ni and Ni/B′ columns, respectively. From the images the B–site order appears to be long–range with no disordered regions or micro–twinning present. However, FFT's corresponding to the HAADF–STEM images of $La_3Ni_2Sb_{0.75}Nb_{0.25}O_9$ and $La_3Ni_2Sb_{0.75}Ta_{0.25}O_9$ taken along various orientations clearly show, see Fig. 10 and Fig. S10, the presence of structured diffuse scattering reminiscent of the diffuse scattering observed [6] in $La_3Ni_2NbO_9$ and $La_3Ni_2TaO_9$. It is likely that the diffuse scattering arises from short range order at the 2*d* site between the 1/3 Ni and 2/3 B' cations but investigating the precise structural modifications responsible for the short–range order is beyond the scope of this paper.

3.2.4. Neutron diffraction

NPD data were collected at room temperature (RT) and 3.5 or 3.0 K for $La_3Ni_2Ta_{0.75}Nb_{0.25}O_9$, $La_3Ni_2Sb_{0.75}Ta_{0.25}O_9$ and $La_3Ni_2Sb_{0.75}Nb_{0.25}O_9$. The data collected at room temperature using $\lambda = 1.622$ Å were consistent with the X–ray and electron diffraction data described above in that they could be accounted for using a monoclinic unit cell with an ordered arrangement of Ni^{2+} and the pentavalent cations. The fits are shown in Fig. S11. Approximately 0.77(6) wt. % of $LaTa_pNb_{1-p}O_4$ was found in $La_3Ni_2Ta_{0.75}Nb_{0.25}O_9$ whereas no secondary phase was detected in the two Sb–containing compounds. The Ni/B' distribution over the two octahedral sites in each perovskite was refined from the data collected at RT and was then held constant during the analysis of the low temperature datasets. At low temperature, extra intensity was present in the 011 reflection of the two Sb–containing samples, $La_3Ni_2Sb_{0.75}Nb_{0.25}O_9$ and $La_3Ni_2Sb_{0.75}Ta_{0.25}O_9$. It could be accounted for by introducing a G–type [11] magnetic structure with the ordered moments aligned along [100]. The magnetic moments of the Ni^{2+} cations on the 2*c* and 2*d* sites were constrained to be equal. They refined to values of 1.18(4) and 1.08(4) μ_B per cation in $La_3Ni_2Sb_{0.75}Nb_{0.25}O_9$ and $La_3Ni_2Sb_{0.75}Ta_{0.25}O_9$, respectively. These values were determined by analysing the diffraction pattern collected using $\lambda = 2.4395$ Å; the atomic parameters were fixed at the values determined in the analysis of the data collected at the same temperature using $\lambda = 1.622$ Å. In contrast, no magnetic Bragg scattering was observed in the diffraction pattern of $La_3Ni_2Ta_{0.75}Nb_{0.25}O_9$ collected at 3.5 K. The patterns recorded at 3.5 K (3 K for $La_3Ni_2Sb_{0.75}Nb_{0.25}O_9$) and the calculated fits are presented in Fig. 11 and Fig. S12 for $\lambda = 2.4395$ and 1.622 Å, respectively, whilst Tables 4–6 list the atomic parameters derived at RT and low temperature for each composition. Selected bond lengths and bond angles are shown in Tables 7 and 8.

4. Discussion

4.1. $La_3Ni_2TaO_9$

The in–field neutron diffraction data shown in Fig. 1 support the hypothesis that $La_3Ni_2TaO_9$ is a relaxor ferromagnet. The observed magnetic Bragg scattering is consistent with the presence of G–type spin

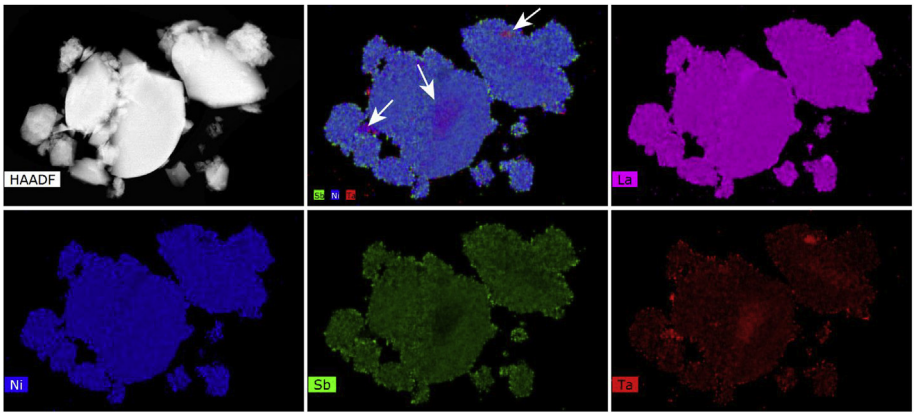

Fig. 5. HAADF–STEM image of particles of $La_3Ni_2Sb_{0.75}Ta_{0.25}O_9$ with a mixed [Ni, Sb, Ta] and individual (La/Ni/Sb/Ta) element maps. The element maps are given in counts. The mixed element map clearly shows regions, marked by arrows, that contain much more Ta and less Sb.

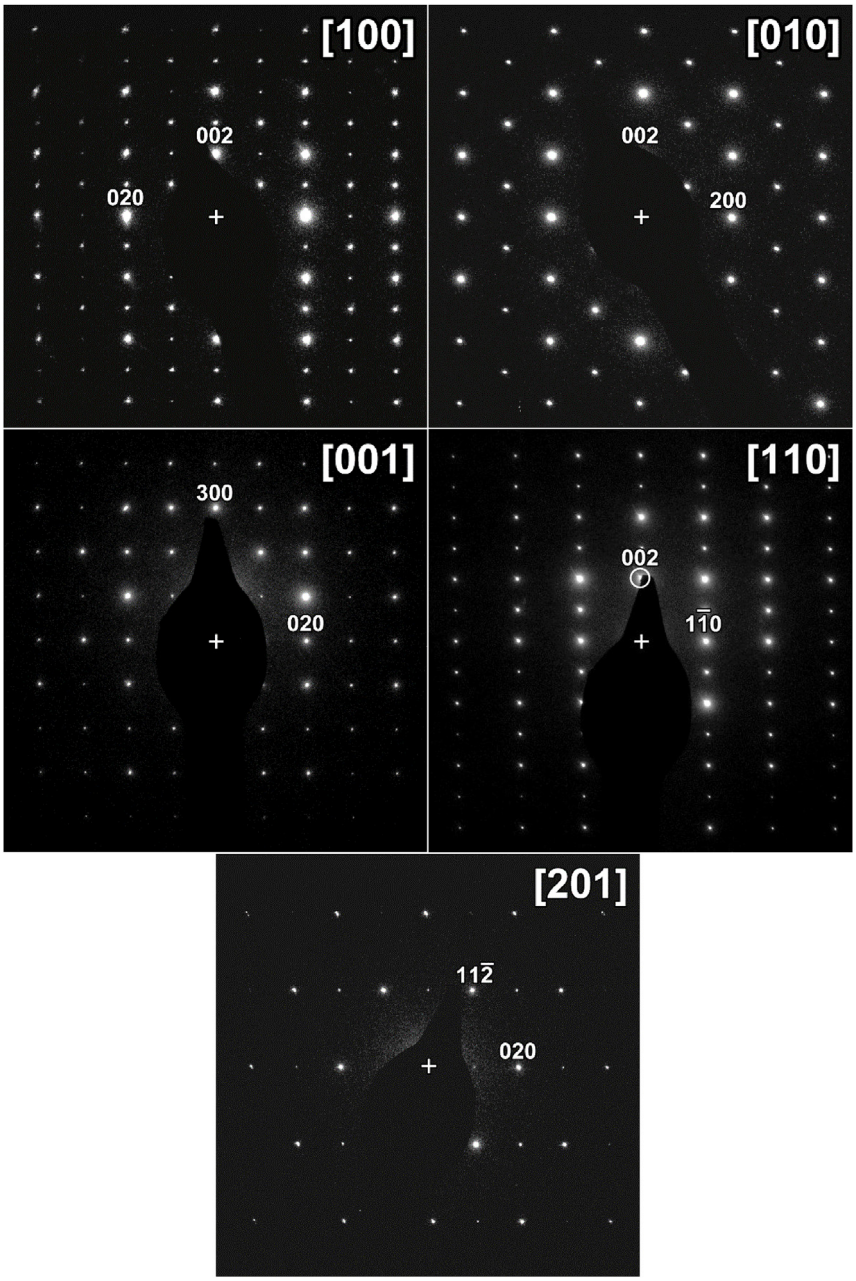

Fig. 6. SAED patterns of the sample $La_3Ni_2Sb_{0.75}Ta_{0.25}O_9$ along the zone axes [100], [010], [001], [110] and [201] corresponding to space group $P2_1/n$.

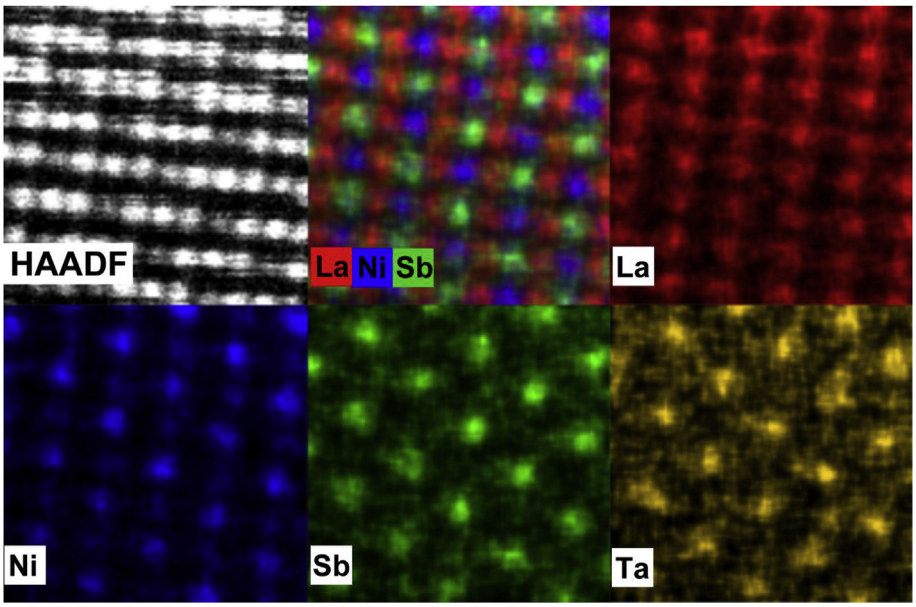

Fig. 7. Atomic resolution EDX map along [010] the zone axis, of $La_3Ni_2Sb_{0.75}Ta_{0.25}O_9$ where La is presented in red and the cations Ni, Sb and Ta in respectively blue, green and yellow. The individual EDX maps of elements Ni, Sb and Ta show ordering between both Ni–Sb and Ni–Ta. (For interpretation of the references to colour in this figure legend, the reader is referred to the Web version of this article.)

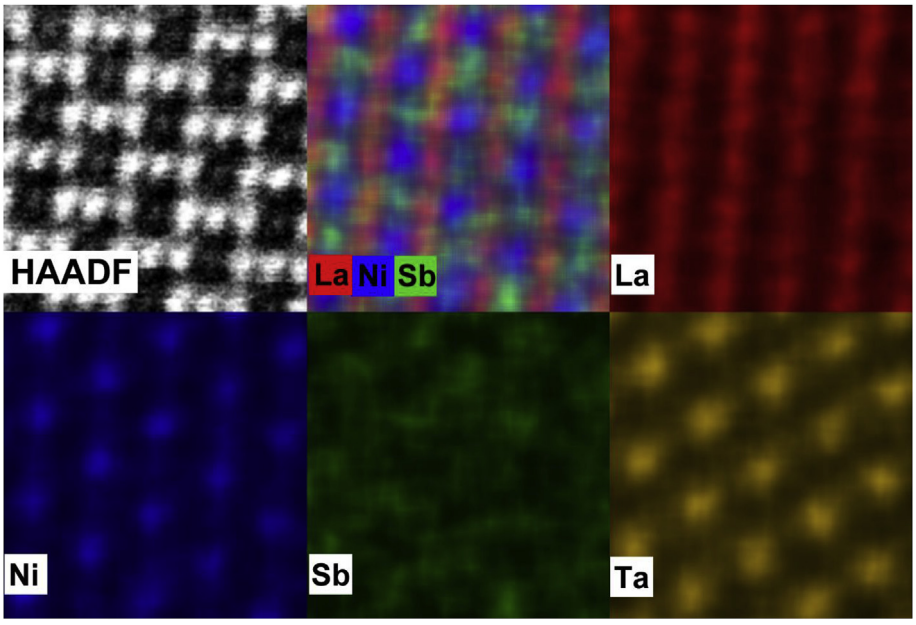

Fig. 8. Atomic resolution EDX map along the [010] zone axis of a region of $La_3Ni_2Sb_{0.75}Ta_{0.25}O_9$ with an inverted composition of Sb and Ta, where La is presented in red and the cations Ni, Sb and Ta in respectively blue, green and yellow. The individual EDX maps of elements Ni, Sb and Ta show ordering between both Ni–Sb and Ni–Ta. (For interpretation of the references to colour in this figure legend, the reader is referred to the Web version of this article.)

ordering although the ordered moment per Ni^{2+} cation in a field of 50 kOe is lower than that of 1.60(3) μ_B induced by the same field in $La_3Ni_2SbO_9$ [5]. However, comparison of $M(H)$ at 5 K for the two compositions shows that the function saturates more slowly in the case of $La_3Ni_2TaO_9$ and the value, 1.34(6) μ_B, determined by neutron diffraction is in excellent agreement with the magnetisation measured by magnetometry at 5 K.

4.2. $La_3Ni_2Sb_xTa_yNb_{1-x-y}O_9$

We have shown that solid solutions containing two different pentavalent cations can be prepared for each of $x = 0$, $y = 0$ and $x + y = 1$. Compositions containing only antimony and tantalum show a strong low–field magnetisation below ~100 K but the introduction of niobium to form either Nb/Sb or Nb/Ta solid solutions decreases both the onset temperature, T_C, and the magnitude of the magnetisation, see Fig. 2 and Tables 1–3. We find this change striking given the similarity in size and charge of Nb^{5+} and Ta^{5+} and in the discussion that follows we consider the structural and electronic factors that might be responsible.

Our X–ray diffraction data suggest that in all cases the cations order over the two six–coordinate sites within the unit cell such that one is predominantly occupied by Ni^{2+} and the other by Ni^{2+} and pentavalent cations in a 1:2 ratio. Neutron diffraction has confirmed this for the three compositions studied in detail. Only in the case of $La_3Ni_2Sb_{0.75}Nb_{0.25}O_9$

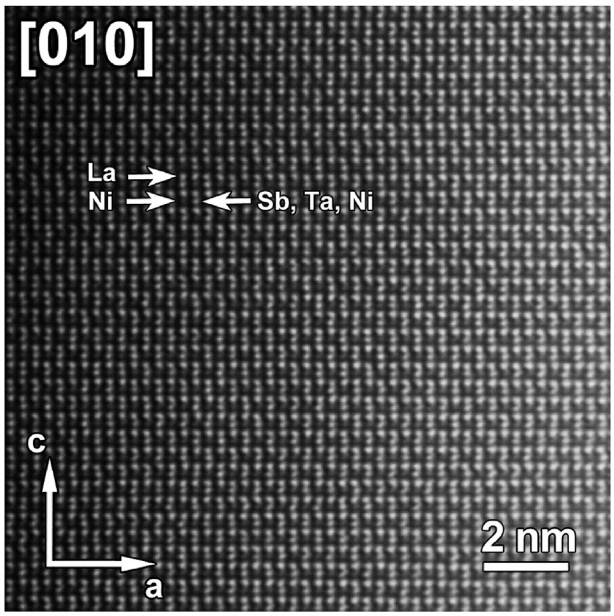

Fig. 9. HAADF–STEM image of the $La_3Ni_2Sb_{0.75}Ta_{0.25}O_9$ sample along the [010] orientation. The rows of bright atomic columns correspond to the A cation La. The rows along the *a*–axis with alternating dark and bright atom columns correspond to Ni and (Sb, Ta and Ni), respectively. In order to reduce the scanning artefacts in the image we have applied a "Gaussian blur" filter.

was the refined concentration of pentavalent cations on the predominantly nickel–occupied 2*c* site significant at the 2σ level, see Table 4. The mean bond length around the nickel–rich 2*c* site at both room temperature and 3.5 K is, as expected, larger than that around the site, 2*d*, containing the smaller, pentavalent cations. As is the case in $La_3Ni_2SbO_9$ and $La_3Ni_2NbO_9$, but not in $La_3Ni_2TaO_9$, the environment around the 2*d* site in each of the three solid solutions expands as that around the 2*c* site contracts. In each case the atomic displacement parameters of some of the oxide ions are large at both room temperature and 3 K, suggesting that the anions show static displacements from their mean positions. The displacement parameters also provide evidence of disorder on the La^{3+} sublattice. The large displacement parameters on both of these sublattices are likely to stem from the different coordination requirements of Ni^{2+} and the pentavalent cations that together occupy the 2*d* site. We note that, contrary to the widely–quoted published data [12], the unit–cell volumes of all [3,6] these compounds suggest that the ionic radius of Sb^{5+} in six–coordination is greater than those of Nb^{5+} and Ta^{5+}.

The results from our electron microscopy study are in broad agreement with those produced by X–ray and neutron diffraction. Furthermore, they show, see Fig. 5, Figs. S5 and S6, that all our samples have the desired overall compositions and that, with the exception of a few local regions, they are homogeneous and monophasic. They also provide, see Fig. 7 and Fig. S8, direct evidence that the pentavalent cations do not occupy the 2*c* sites but that they are randomly distributed over the 2*d* sites. The long–range nature of the 2*c*/2*d* cation ordering is emphasised by Fig. 9 and Fig. S9. Finally, the diffuse scattering in the diffraction patterns generated by taking the Fourier transform of the HAADF–STEM images, see Fig. 10 and Fig. S10, indicates the presence of short–range structural ordering that is not included in the model derived from our neutron diffraction data. Similar diffuse scattering was observed in our previous study of $La_3Ni_2TaO_9$ and $La_3Ni_2NbO_9$ [6]. Further experimental work will be necessary before we can fully explain the origin of this scattering.

We have previously described $La_3Ni_2TaO_9$ as a relaxor ferromagnet

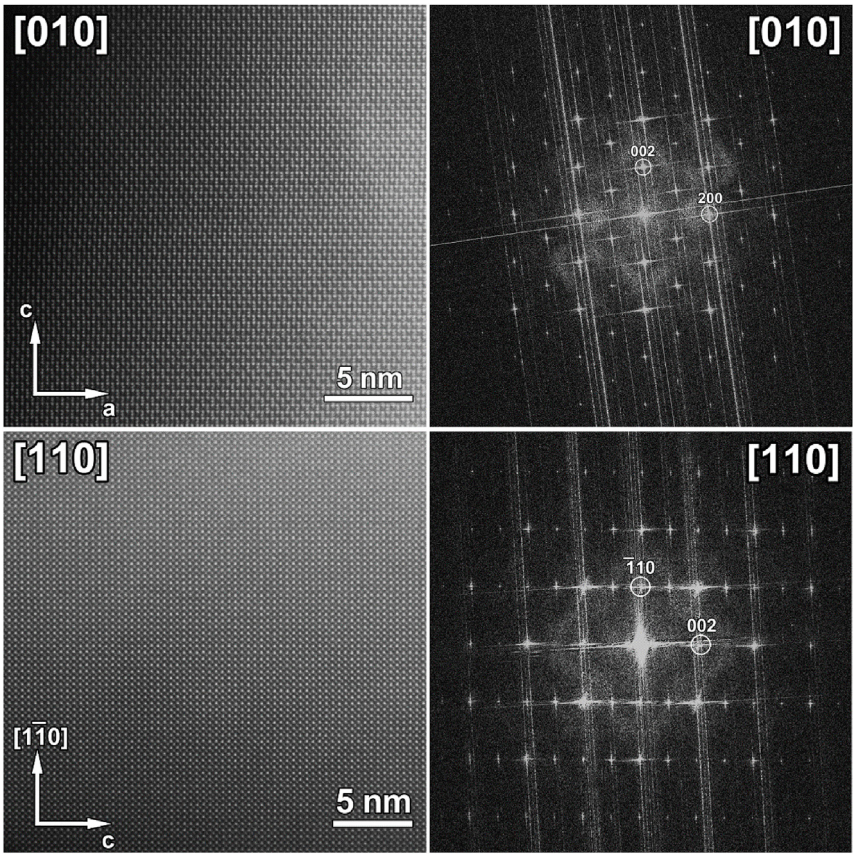

Fig. 10. Left: HAADF–STEM image along the [010] and [110] zone axes of the $La_3Ni_2Sb_{0.75}Ta_{0.25}O_9$ sample, where B cation ordering is clearly present. Right: corresponding FFTs, in which diffuse intensities are observed.

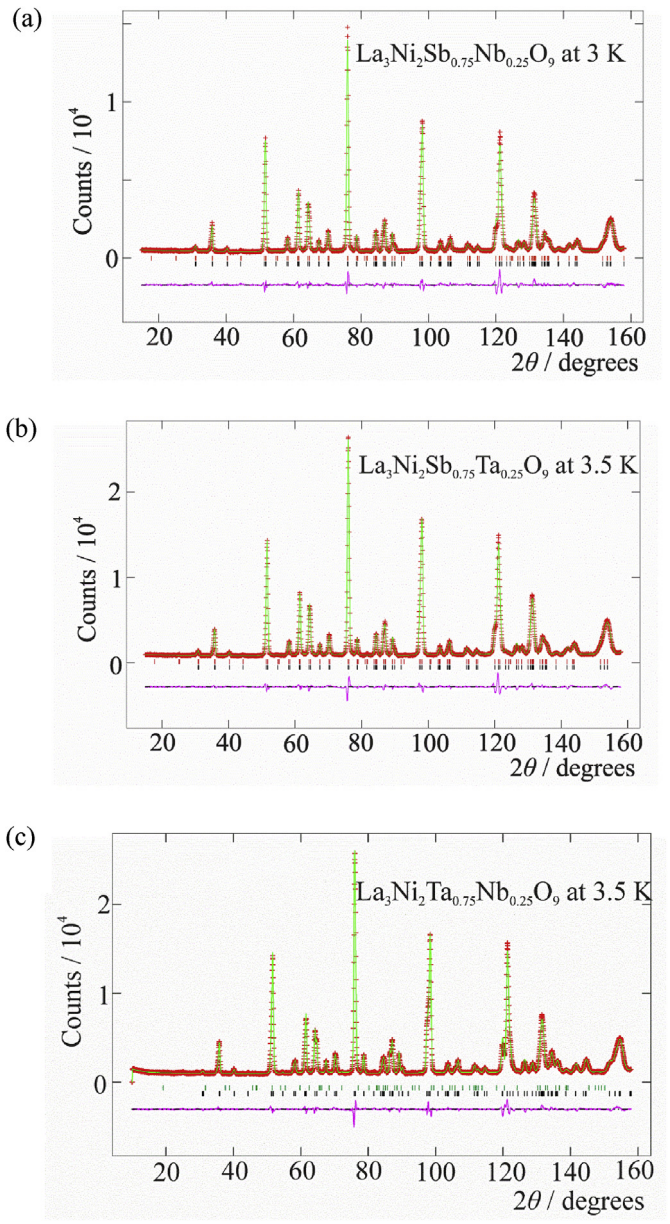

Fig. 11. Observed (red crosses) and calculated (green line) NPD profiles of (a) $La_3Ni_2Sb_{0.75}Nb_{0.25}O_9$, (b) $La_3Ni_2Sb_{0.75}Ta_{0.25}O_9$ and (c) $La_3Ni_2Ta_{0.75}Nb_{0.25}O_9$ at 3 K recorded using $\lambda = 2.4395$ Å. A difference curve (purple) is shown below. Reflection markers are shown for the magnetic (red) and structural (black) phases and for any $LaTaO_4$ impurity (green). (For interpretation of the references to colour in this figure legend, the reader is referred to the Web version of this article.)

and $La_3Ni_2SbO_9$ as a relaxor ferromagnet in which some of the domains are large enough for the magnetic ordering to be detected by zero–field neutron diffraction [5], albeit with a low mean magnetic moment, 0.89(7) μ_B, for the Ni^{2+} cations. The magnetometry and in–field neutron diffraction data described above suggest that relaxor behaviour persists throughout the $La_3Ni_2Sb_xTa_yO_9$ ($x + y = 1$) solid solution. Our neutron diffraction data show that the large domains are still present when $x = 0.75$, albeit with a slightly lower mean moment per cation, but our previous study of $La_3Ni_2TaO_9$ showed that they are absent for $x = 0$. It is thus possible that these domains are responsible for the relatively sharp transition seen at ~100 K in the ac susceptibility of both $La_3Ni_2SbO_9$ [3] and $La_3Ni_2Sb_{0.75}Ta_{0.25}O_9$, see Fig. 4, but not in that of $La_3Ni_2TaO_9$ [6]. The introduction of 75% Ta^{5+} reduces the magnetisation of $La_3Ni_2SbO_9$ in 100 Oe by only ~25%, see Fig. 2, but there is then a threefold

Table 4
Structural parameters of $La_3Ni_2Sb_{0.75}Nb_{0.25}O_9$ at RT and 3 K (Space group $P2_1/n$).

		RT	3 K
a/Å		5.5993(1)	5.5891(1)
b/Å		5.6374(1)	5.6353(1)
c/Å		7.9286(2)	7.9165(2)
β/°		90.03(1)	90.08(1)
V/Å^3		250.27(1)	249.34(1)
R_{wp}/%		4.33	4.61
χ^2		2.243	2.617
La	x	0.4900(6)	0.4901(5)
4*e* (x y z)	y	0.4616(2)	0.4600(2)
	z	0.252(1)	0.249(1)
	U_{ISO}/Å^2	0.0186(4)	0.0146(3)
Ni/Sb/Nb1	U_{ISO}/Å^2	0.0033(2)	0.0011(2)
2*c* (0 ½ 0)	Ni occupancy	0.96(2)	0.96
	Sb occupancy	0.03(2)	0.03
	Nb occupancy	0.010(5)	0.010
Ni/Sb/Nb2	U_{ISO}/Å^2	0.0033(2)	0.0011(2)
2*d* (½ 0 0)	Ni occupancy	0.37(2)	0.37
	Sb occupancy	0.47(2)	0.47
	Nb occupancy	0.156(5)	0.156
O1	x	0.790(1)	0.786(1)
4*e* (x y z)	y	0.7930(9)	0.798(1)
	z	−0.0369(6)	−0.0411(8)
	U_{ISO}/Å^2	0.0024(11)	0.0025(12)
O2	x	0.711(1)	0.705(1)
4*e* (x y z)	y	0.284(1)	0.283(1)
	z	−0.0464(7)	−0.0419(8)
	U_{ISO}/Å^2	0.017(1)	0.007(1)
O3	x	0.5773(5)	0.5798(5)
4*e* (x y z)	y	0.0176(4)	0.0176(3)
	z	0.244(1)	0.247(1)
	U_{ISO}/Å^2	0.0121(5)	0.0075(5)

Table 5
Structural parameters of $La_3Ni_2Sb_{0.75}Ta_{0.25}O_9$ at RT and 3.5 K (Space group $P2_1/n$).

		RT	3.5 K
a/Å		5.6010(1)	5.5907(1)
b/Å		5.6369(1)	5.6344(1)
c/Å		7.9299(2)	7.9178(2)
β/°		90.00(1)	90.02(1)
V/Å^3		250.37(1)	249.41(1)
R_{wp}/%		4.13	3.69
χ^2		2.650	3.287
La	x	0.4897(6)	0.4913(4)
4*e* (x y z)	y	0.4620(2)	0.4599(2)
	z	0.252(1)	0.251(1)
	U_{ISO}/Å^2	0.0183(3)	0.0149(2)
Ni/Sb/Ta1	U_{ISO}/Å^2	0.0032(2)	0.0007(1)
2*c* (0 ½ 0)	Ni occupancy	0.99(2)	0.99
	Sb occupancy	0.01(1)	0.01
	Ta occupancy	0.003(4)	0.003
Ni/Sb/Ta2	U_{ISO}/Å^2	0.0032(2)	0.0007(1)
2*d* (½ 0 0)	Ni occupancy	0.35(2)	0.35
	Sb occupancy	0.49(1)	0.49
	Ta occupancy	0.163(4)	0.163
O1	x	0.785(1)	0.780(1)
4*e* (x y z)	y	0.788(1)	0.796(1)
	z	−0.0479(6)	−0.0451(6)
	U_{ISO}/Å^2	0.0152(15)	0.0081(13)
O2	x	0.707(1)	0.701(1)
4*e* (x y z)	y	0.290(1)	0.286(1)
	z	−0.0346(5)	−0.0406(7)
	U_{ISO}/Å^2	0.004(1)	0.0006(15)
O3	x	0.5796(6)	0.5779(4)
4*e* (x y z)	y	0.0169(4)	0.0173(3)
	z	0.242(1)	0.251(1)
	U_{ISO}/Å^2	0.0125(5)	0.0087(4)

reduction as the remaining antimony is removed. However, the maximum dc susceptibility of $La_3Ni_2TaO_9$ is an order of magnitude

Table 6
Structural parameters of $La_3Ni_2Ta_{0.75}Nb_{0.25}O_9$ at RT and 3.5 K (Space group $P2_1/n$).

		RT	3.5 K
a/Å		5.5890(1)	5.5777(1)
b/Å		5.6415(1)	5.6406(1)
c/Å		7.9193(2)	7.9063(1)
β/°		90.04(1)	90.03(1)
V/Å^3		249.70(1)	248.75(1)
R_{wp}/%		4.04	3.11
χ^2		2.539	2.555
La	x	0.4909(5)	0.4914(4)
4*e* (*x y z*)	y	0.4612(2)	0.4587(1)
	z	0.255(1)	0.250(1)
	U_{ISO}/Å^2	0.0181(3)	0.0144(2)
Ni/Ta/Nb1	U_{ISO}/Å^2	0.0023(2)	0.0006(1)
2*c* (0 ½ 0)	Ni occupancy	1	1
	Ta occupancy	0	0
	Nb occupancy	0	0
Ni/Ta/Nb2	U_{ISO}/Å^2	0.0023(2)	0.0006(1)
2*d* (½ 0 0)	Ni occupancy	0.3333	0.3333
	Ta occupancy	0.5	0.5
	Nb occupancy	0.1667	0.1667
O1	x	0.783(1)	0.793(1)
4*e* (*x y z*)	y	0.786(1)	0.797(1)
	z	−0.0422(8)	−0.0384(6)
	U_{ISO}/Å^2	0.0037(12)	0.0012(10)
O2	x	0.700(1)	0.711(1)
4*e* (*x y z*)	y	0.294(1)	0.285(1)
	z	−0.0393(7)	−0.0450(6)
	U_{ISO}/Å^2	0.0121(11)	0.0059(11)
O3	x	0.5783(5)	0.5787(3)
4*e* (*x y z*)	y	0.0173(4)	0.0175(3)
	z	0.241(1)	0.251(1)
	U_{ISO}/Å^2	0.0138(6)	0.0083(4)

Table 7
Selected bond lengths (Å) and angles (°) in $La_3Ni_2Sb_xTa_yNb_{1-x-y}O_9$ at RT.

	$La_3Ni_2Sb_{0.75}Nb_{0.25}O_9$	$La_3Ni_2Sb_{0.75}Ta_{0.25}O_9$	$La_3Ni_2Ta_{0.75}Nb_{0.25}O_9$
La–O1	2.741(9)	2.836(9)	2.782(9)
La–O1	2.726(8)	2.643(8)	2.670(8)
La–O1	2.442(7)	2.410(8)	2.441(7)
La–O2	2.854(10)	2.757(8)	2.776(8)
La–O2	2.447(8)	2.479(7)	2.443(7)
La–O2	2.628(9)	2.717(7)	2.713(6)
La–O3	2.551(3)	2.560(3)	2.554(3)
La–O3	2.443(4)	2.433(4)	2.429(4)
2*c* – O1	2.050(5) × 2	2.054(7) × 2	2.048(5) × 2
2*c* – O2	2.059(6) × 2	2.040(5) × 2	2.062(4) × 2
2*c* – O3	2.078(9) × 2	2.098(10) × 2	2.103(9) × 2
2*d* – O1	2.019(5) × 2	2.033(6) × 2	2.016(4) × 2
2*d* – O2	2.022(6) × 2	2.025(5) × 2	2.026(5) × 2
2*d* – O3	1.985(9) × 2	1.971(10) × 2	1.957(8) × 2
O1 –2*c*–O2	90.0(3) × 2	87.8(3) × 2	86.4(3) × 2
O1– 2*c* –O3	88.9(2) × 2	88.8(2) × 2	90.0(2) × 2
O2 – 2*c* –O3	87.8(2) × 2	89.3(2) × 2	89.8(2) × 2
O1 – 2*d* – O2	87.8(3) × 2	90.0(3) × 2	88.2(3) × 2
O1 – 2*d* – O3	89.7(2) × 2	88.1(2) × 2	89.0(2) × 2
O2 – 2*d* – O3	89.4(2) × 2	87.9(2) × 2	89.2(2) × 2
2*c* – O1 – 2*d*	155.0(3)	152.9(3)	155.5(3)
2*c* – O2 – 2*d*	153.5(3)	155.6(3)	152.5(3)
2*c* – O3 – 2*d*	154.7(2)	154.1(2)	154.4(1)

Table 8
Selected bond lengths (Å) and angles (°) in $La_3Ni_2Sb_xTa_yNb_{1-x-y}O_9$ at low T.

	$La_3Ni_2Sb_{0.75}Nb_{0.25}O_9$	$La_3Ni_2Sb_{0.75}Ta_{0.25}O_9$	$La_3Ni_2Ta_{0.75}Nb_{0.25}O_9$
La–O1	2.780(10)	2.811(9)	2.732(8)
La–O1	2.684(8)	2.654(8)	2.720(7)
La–O1	2.433(9)	2.427(9)	2.433(7)
La–O2	2.785(10)	2.770(9)	2.813(8)
La–O2	2.445(9)	2.446(9)	2.449(7)
La–O2	2.675(9)	2.697(8)	2.638(7)
La–O3	2.543(2)	2.541(2)	2.536(2)
La–O3	2.426(4)	2.430(3)	2.421(3)
2*c* – O1	2.083(5) × 2	2.101(5) × 2	2.057(4) × 2
2*c* – O2	2.081(4) × 2	2.086(5) × 2	2.049(5) × 2
2*c* – O3	2.052(7) × 2	2.023(8) × 2	2.021(8) × 2
2*d* – O1	1.994(4) × 2	1.976(5) × 2	2.018(4) × 2
2*d* – O2	1.990(5) × 2	1.991(6) × 2	2.024(4) × 2
2*d* – O3	2.011(7) × 2	2.035(8) × 2	2.033(9) × 2
O1 –2*c*–O2	89.7(3) × 2	87.9(3) × 2	89.2(3) × 2
O1– 2*c* –O3	89.3(2) × 2	89.9(2) × 2	89.0(2) × 2
O2 – 2*c* –O3	89.4(2) × 2	89.7(2) × 2	88.5(2) × 2
O1 – 2*d* – O2	88.2(3) × 2	89.7(3) × 2	87.4(3) × 2
O1 – 2*d* – O3	89.4(2) × 2	88.0(2) × 2	90.0(1) × 2
O2 – 2*d* – O3	89.8(2) × 2	89.9(2) × 2	89.6(2) × 2
2*c* – O1 – 2*d*	153.5(3)	153.5(3)	153.4(3)
2*c* – O2 – 2*d*	154.3(4)	153.5(3)	153.8(3)
2*c* – O3 – 2*d*	154.0(1)	154.6(1)	154.4(1)

greater than that of the niobium analogue. Both neutron diffraction and ac magnetometry show that large magnetic domains are also present in $La_3Ni_2Sb_{0.75}Nb_{0.25}O_9$ and the temperature dependence and magnitude of the dc susceptibility suggests that relaxor behaviour persists in the 1:1 Sb:Nb composition. However, the introduction of 75% Nb^{5+} into $La_3Ni_2SbO_9$ reduces the magnetisation in 100 Oe by ~75%. It appears that the magnetisation is maximised by the presence of antimony, largely maintained after the introduction of tantalum and reduced markedly by the introduction of niobium. Furthermore, the magnetisation is largest when relatively large domains form.

The absence of magnetic Bragg scattering in the neutron diffraction pattern of $La_3Ni_2Ta_{0.75}Nb_{0.25}O_9$ recorded at 3.5 K signals the absence of large magnetic domains and is consistent with the data collected previously from $La_3Ni_2TaO_9$ and $La_3Ni_2NbO_9$. On the basis of the data presented previously and above, we believe the former member of this pair to be a relaxor ferromagnet and the latter to be a spin glass. The change in behaviour with composition thus entails a progression from short–range magnetic ordering, albeit in domains too small to be detected by neutron diffraction, to an absence of magnetic ordering. The susceptibility data in Figs. 2 and 4 suggest that the introduction of 25% niobium in place of tantalum is not sufficient to change the nature of the compound. However, the data in Table 3, along with Figs. 2 and 3 and Fig. S4, suggest that a change in the low–temperature behaviour of $La_3Ni_2Ta_yNb_{1-y}O_9$ begins in the composition range $0.5 < y < 0.75$. We note that the parameters describing the behaviour of this series in the paramagnetic region are essentially constant across the entire composition range. As described above, the data collected on other compositions suggest that the short–range magnetic ordering is likely to involve the presence of ferrimagnetic G–type domains in which nearest–neighbour interactions dominate. The formation of a spin glass requires the presence of magnetic frustration, which in turn implies that a second superexchange interaction must increase in importance and compete with the nearest–neighbour interaction as the concentration of niobium increases. This interaction, which must be uncompetitive in $La_3Ni_2SbO_9$ and $La_3Ni_2TaO_9$, could be either the second–nearest–neighbour interaction along an approximately 90° Ni – O – *B*' – O – Ni pathway, with a direct Ni – Ni

distance of ~5.5 Å, or the third–nearest–neighbour interaction along a nearly–linear Ni – O – B' – O – Ni pathway of length ~7.8 Å. The adoption of a Type I antiferromagnetic structure by $SrLaNiSbO_6$ [13] shows that the former pathway can be significant when B' = Sb, but it has also been shown [14–16] that the $4d^{10}$ shell of post–transition metals is too low in energy to play a part in the interaction, which therefore effectively takes place along a Ni – O – O – Ni pathway and so can operate whatever the identity of B'. However, the nearly–linear Ni – O – B' – O – Ni pathway can only operate with the participation of orbitals on the B′ cation and so could be significant for $B' = d^0$ Nb^{5+} or Ta^{5+}, but not when $B' = Sb^{5+}$. In order to explain the greater significance of the competitive interaction in the niobium–rich compositions we tentatively suggest that the energy of the empty 4*d* orbitals of Nb^{5+} is relatively close to that of the anion orbitals and they are therefore able to participate effectively in the linear superexchange but that the $5d^0$ orbitals of Ta^{5+} lie too high in energy to participate to the same degree. Consequently the magnetic frustration increases with increasing niobium content and $La_3Ni_2NbO_9$ adopts a spin–glass state at low temperatures. The competing superexchange interaction present in $La_3Ni_2TaO_9$ is not enough to prevent the formation of a relaxor state but the third–nearest–neighbour coupling might be strong enough to reduce both the size of the domains formed and the ordered moment measured by neutron diffraction. There may also be a structural difference that has consequences for the magnetic properties. More specifically, it has been shown [17] that Nb^{5+} is more likely to move away from the centre of the coordination octahedron than is Ta^{5+}. In the compounds under discussion any such displacements would be local rather than cooperative, but they might still be partially responsible for the differences in the magnetic behaviour. It is interesting that the imaginary components of the ac susceptibilities of the antimony–containing, large–domain compositions show a change in gradient, see Fig. 4, at the temperature at which those of the relaxor phases that do not contain large domains, i.e. $La_3Ni_2TaO_9$ and $La_3Ni_2Ta_{0.75}Nb_{0.25}O_9$, reach a maximum. This suggests that some regions of the sample order at ~100 K and that smaller regions follow suite at lower temperatures. Neutron scattering experiments to identify short–range atomic ordering and to determine the spin correlation length in these materials as a function of temperature are underway.

5. Conclusion

The results of our in–field neutron diffraction experiment support the proposal that $La_3Ni_2TaO_9$, like $La_3Ni_2SbO_9$, is a relaxor ferromagnet. Magnetometry and neutron diffraction have shown that this behaviour persists in the solid solution $La_3Ni_2Sb_xTa_yNb_{1-x-y}O_9$ when $x + y = 1$ although the magnitude of the magnetisation decreases as *y* increases. However, the introduction of niobium causes a relatively rapid decrease in both the magnetisation and the onset temperature and eventually leads to the formation of a spin–glass phase when $x = y = 0$. Neutron diffraction and electron microscopy showed our samples to be well–ordered and homogeneous; there are no structural differences that might explain the magnetic changes that occur when niobium is introduced. The energies of the outer *d* orbitals of the pentavalent cations determine the ability of these cations to play a role in superexchange interactions and we propose that the differences in the *d*–orbital energies for Sb^{5+}, Nb^{5+} and Ta^{5+} are responsible for the observed variations in magnetic behaviour.

Acknowledgments

We thank EPSRC for funding through grant EP/M0189541. CMC thanks the Croucher Foundation and the University of Oxford for the award of a graduate scholarship.

Appendix A. Supplementary data

Supplementary data to this article can be found online at https://doi.org/10.1016/j.jssc.2019.02.044.

References

[1] R. Paria Sena, J. Hadermann, C.M. Chin, E.C. Hunter, P.D. Battle, J. Solid State Chem. 243 (2016) 304–311.
[2] E.C. Hunter, P.D. Battle, R. Paria Sena, J. Hadermann, J. Solid State Chem. 248 (2017) 96–103.
[3] P.D. Battle, S.I. Evers, E.C. Hunter, M. Westwood, Inorg. Chem. 52 (2013) 6648.
[4] A.A. Bokov, Z.G. Ye, J. Mater. Sci. 41 (2006) 31–52.
[5] P.D. Battle, M. Avdeev, J. Hadermann, J. Solid State Chem. 220 (2014) 163.
[6] C.M. Chin, P.D. Battle, S.J. Blundell, E. Hunter, F. Lang, M. Hendrickx, R.P. Sena, J. Hadermann, J. Solid State Chem. 258 (2018) 825–834.
[7] K. Dey, A. Indra, D. De, S. Majumdar, S. Giri, ACS Appl. Mater. Interfaces 8 (2016) 12901–12907.
[8] M. Avdeev, J.R. Hester, J. Appl. Crystallogr. 51 (2018) 1597–1604.
[9] H.M. Rietveld, J. Appl. Crystallogr. 2 (1969) 65–71.
[10] A.C. Larson, R.B. von-Dreele, General Structure Analysis System (GSAS), LAUR 86-748, Los Alamos National Laboratories, 1994.
[11] E.O. Wollan, W.C. Koehler, Phys. Rev. 100 (1955) 545–563.
[12] R.D. Shannon, Acta Crystallogr. A 32 (1976) 751.
[13] M.P. Attfield, P.D. Battle, S.K. Bollen, T.C. Gibb, R.J. Whitehead, J. Solid State Chem. 100 (1992) 37.
[14] O. Mustonen, S. Vasala, E. Sadrollahi, K.P. Schmidt, C. Baines, H.C. Walker, I. Terasaki, F.J. Litterst, E. Baggio-Saitovitch, M. Karppinen, Nat. Commun. 9 (2018).
[15] Y.H. Xu, S.S. Liu, N.R. Qu, Y.L. Cui, Q.Q. Gao, R.N. Chen, J. Wang, F.M. Gao, X.F. Hao, J. Phys. Condens. Matter 29 (2017).
[16] M. Zhu, D. Do, C.R. Dela Cruz, Z. Dun, H.D. Zhou, S.D. Mahanti, X. Ke, Phys. Rev. Lett. 113 (2014) 5.
[17] K.M. Ok, P.S. Halasyamani, D. Casanova, M. Llunell, P. Alemany, S. Alvarez, Chem. Mater. 18 (2006) 3176–3183.